



Cite this: DOI: 10.1039/c7lc01211j

## Integrated dual-modality microfluidic sensor for biomarker detection using lithographic plasmonic crystal†

Md. Azahar Ali,  ‡ Shawana Tabassum,  ‡ Qiugu Wang, Yifei Wang, Ratnesh Kumar and Liang Dong\*

This paper reports an integrated dual-modality microfluidic sensor chip, consisting of a patterned periodic array of nanoposts coated with gold (Au) and graphene oxide (GO), to detect target biomarker molecules in a limited sample volume. The device generates both electrochemical and surface plasmon resonance (SPR) signals from a single sensing area of Au–GO nanoposts. The Au–GO nanoposts are functionalized with specific receptor molecules, serving as a spatially well-defined nanostructured working electrode for electrochemical sensing, as well as a nanostructured plasmonic crystal for SPR-based sensing *via* the excitation of surface plasmon polaritons. High sensitivity of the electrochemical measurement originates from the presence of the nanoposts on the surface of the working electrode where radial diffusion of redox species occurs. Complementarily, the SPR detection allows convenient tracking of dynamic antigen–antibody interactions, to describe the association and dissociation phases occurring at the sensor surface. The soft-lithographically formed nanoposts provide high reproducibility of the sensor response to epidermal growth factor receptor (*ErbB2*) molecules even at a femtomolar level. Sensitivities of the electrochemical measurements to *ErbB2* are found to be  $20.47 \mu\text{A} \mu\text{M}^{-1} \text{cm}^{-2}$  in a range from 1 fM to 0.1  $\mu\text{M}$ , and those of the SPR measurements to be  $1.35 \text{ nm} \mu\text{M}^{-1}$  in a range from 10 pM to 1 nM, and  $0.80 \text{ nm} \mu\text{M}^{-1}$  in a range from 1 nM to 0.1  $\mu\text{M}$ . The integrated dual-modality sensor offers higher sensitivity (through higher surface area and diffusions from nanoposts for electrochemical measurements), as well as the dynamic measurements of antigen–antibody bindings (through the SPR measurement), while operating simultaneously in a same sensing area using the same sample volume.

Received 12th November 2017,  
Accepted 8th February 2018

DOI: 10.1039/c7lc01211j

rsc.li/loc

## 1. Introduction

Conventional tools for diagnosis of cancerous tissues include X-ray mammography, magnetic resonance imaging (MRI), enzyme-linked immunosorbent assay (ELISA), and immunohistochemistry.<sup>1–4</sup> However, ~80% of most breast cancers may not be detected by the mammographic screening method due to highly dense and proliferative cells.<sup>2</sup> The MRI method is relatively expensive, and cancerous features may not be detected until they are large enough to be imaged. The ELISA and immunohistochemistry methods require large volumes of samples and tagging molecules.<sup>3,4</sup> In this context, high-performance miniaturized sensors with minute sample consumptions are highly desirable. Recently, many reported microfluidic sensors have demonstrated their ability to detect

cancer biomarkers with high sensitivity.<sup>5,6</sup> An example of a cancer biomarker is the epidermal growth factor receptor (*ErbB*), a cell-surface receptor in humans that regulates cell proliferation, migration, apoptosis, and motility *via* different signaling pathways.<sup>7,8</sup> Excessive signaling of *ErbB* is associated with the malignancy of tumors and neurodegenerative diseases. Among *ErbB* genes, the amplification (~30%) of *ErbB2* gene, which encodes a transmembrane glycoprotein, is responsible for breast cancer metastasis.<sup>9</sup> Breast cancers can have up to 25–50 copies of the *ErbB2* gene and up to 40–100-fold increase in *ErbB2* protein, leading to 2 million receptors expressed at the tumor cell surface.<sup>10</sup>

Most of the cancer biomarker-based sensors provide a single modality of electrical, mechanical, electrochemical, or optical signal. With the continuing trend of minimizing sample consumptions, there is an issue with reliability and accuracy of the miniaturized sensors for biomarker detection associated with using limited sample volumes. Therefore, several efforts have been made to tackle this problem, including creating nanofluidic structures to handle reduced volumes of sample, agent and reagent,<sup>11</sup> developing new receptor

Department of Electrical and Computer Engineering, Iowa State University, Ames, Iowa 50011, USA. E-mail: ldong@iastate.edu; Fax: +1 515 294 0388

† Electronic supplementary information (ESI) available. See DOI: 10.1039/c7lc01211j

‡ Authors contributed equally to this work.

molecules with improved detection specificity,<sup>12</sup> enhancing surface areas of sensing materials,<sup>13</sup> and tracking spectral shifts of multiple resonance peaks of optical sensors.<sup>14</sup>

Generation and monitoring of different sensing modalities from a single sensor has also been demonstrated to improve detection reliability and reduce false reads of the sensor.<sup>15,16</sup> In this work, we report a dual-modality sensor that integrates the electrochemical and surface plasmon resonance (SPR) modalities in a novel way, on the same sensing surface, offering the opportunity to work with same sample volume for both the modalities.

Notably, electrochemical sensors allow high-sensitivity detection of cancer biomarkers,<sup>17</sup> and many micro/nanostructured conducting materials are incorporated into electrochemical sensors for improving the surface area to volume ratio, electron transport rate, and electrochemical reactivity of the working electrodes.<sup>18</sup> These improved electrodes enable more efficient radial or spherical diffusions of redox species from surrounding bulk solutions to electrode surfaces, compared to the linear diffusion occurring at a planar or macroscale electrode.<sup>19–21</sup> Consequently, nanomaterials with different shapes (*e.g.*, disk, cylindrical, band, ring, *etc.*)<sup>19–21</sup> have been developed using various methods, such as nanoparticles by *in situ* chemical synthesis,<sup>22</sup> nanowires by hydrothermal synthesis,<sup>23</sup> nanotubes by chemical vapor deposition,<sup>24</sup> and patterned nanofibers by electrospinning.<sup>25,26</sup>

Similarly, plasmonic biosensors have also been extensively reported to detect cancer biomarkers,<sup>27</sup> and study bimolecular interactions of receptor–ligand,<sup>28</sup> avidin–biotin,<sup>29</sup> protein–DNA,<sup>30</sup> and protein–protein.<sup>31</sup> Essentially, this type of optical sensor detects subtle changes in refractive index caused by the immobilization and binding of biomolecules at the surface of noble metal-based nanostructures. It should be noted that, although many metallic nanostructures have been applied to plasmonic biosensors, they are often realized using non-lithographical approaches with a relatively low spatial uniformity in size, shape and distribution. This has influenced the performance reproducibility of these sensors.<sup>32,33</sup> To obtain high uniformity, advanced nanofabrication techniques, such as electron-beam lithography,<sup>34</sup> focused ion beam lithography,<sup>35</sup> nanoimprinting,<sup>36</sup> multiphoton lithography,<sup>37</sup> and hole mask lithography,<sup>38</sup> have been adopted to realize well-defined nanostructures (*e.g.*, nanogratings,<sup>39</sup> nanoholes,<sup>40</sup> nanocones,<sup>41</sup> and nanoposts<sup>36,42</sup>) for plasmonic biosensors. It is also noted that besides plasmonic sensors, other optical sensors, such as ring resonators,<sup>43</sup> one-dimensional (1D) distributed feedback gratings,<sup>44</sup> photonic crystal (PC) cavities,<sup>45</sup> and Raman spectroscopic-based devices,<sup>46</sup> have also been developed to detect various chemical and biological species. For example, low limit of detection and high sensitivity have been demonstrated using the PC cavity-based biosensor due to the ability of the PC defect cavity to strongly confine light which causes narrow resonant modes.<sup>47</sup>

Here we report our integrated dual-modality microfluidic sensor combining the two aforementioned sensing modalities, namely, electrochemical and plasmonic measurements,

on a single nanostructured substrate to detect cancer biomarker in a small sample volume (Fig. 1a and b). The periodically arranged nanoposts coated with a gold–graphene oxide (Au–GO) layer serve as the working electrode of an electrochemical sensor, as well as the nanopatterned substrate of a plasmonic sensor. Because the nanoposts are manufactured using a soft lithography based nanomolding process, they are inexpensive and have high structural uniformity and thus provide improved performance reproducibility of the sensors. Further, due to the presence of the nanoposts on the working electrode that provides a larger surface area, the electrochemical signal produced from the sensor is greater than its counterpart using a planar electrode.

While electrochemical sensors offer high sensitivity, they are generally limited in the dynamic tracking of binding kinetics (*e.g.*, equilibrium association and dissociation phases) of biomolecular interactions at the sensor surface.<sup>48,49</sup> This limitation is overcome by our plasmonic sensing performed on the same nanopost area that excels in tracking dynamic antigen–antibody interactions. Such an ability allows quantifying of protein–protein binding affinity for studying binding kinetics, which, in general, is crucial to help understand molecular recognition of the biological system, and thus help design and implement a better target antibody for antigen.<sup>50</sup> Therefore, the combination of the electrochemical and plasmonic sensing modalities together in the same area on a single nanostructured substrate offer both sensitivity and quantitative information of biomolecular interactions, in addition to other advantages such as small footprint area, low sample consumption, and improved detection reliability.

Compared to our previous work,<sup>51</sup> the contributions of this work are as follows:

- Detailed fabrication process for the integrated dual-modality sensor.
- Electrochemical simulation to illustrate the importance of using Au-coated nanoposts, chronoamperometry (CA) and cyclic voltammetry (CV) studies of the sensor, and demonstration of detection for the breast cancer biomarker *ErbB2*.
- Complete characterization of sensitivity, selectivity, reproducibility, and stability for electrochemical measurement.
- Simulation and analysis of SPR mode of the sensor, and estimation of sensitivity to changes in surrounding refractive index.
- SPR measurement for *ErbB2* with sensitivity, reproducibility, and stability, and demonstration of using the SPR mode to monitor binding kinetics at the sensor surface continuously.
- Demonstration of simultaneously using both the electrochemical and SPR measurement methods on a single dual-modality sensor to detect *ErbB2*.
- Performance comparisons of the sensor with existing sensors reported in the literature for the detection of *ErbB2*.

## 2. Sensor structure and fabrication

### 2.1. Structure

The periodically arranged Au–GO nanoposts serve as the working electrode for the electrochemical sensor, and also

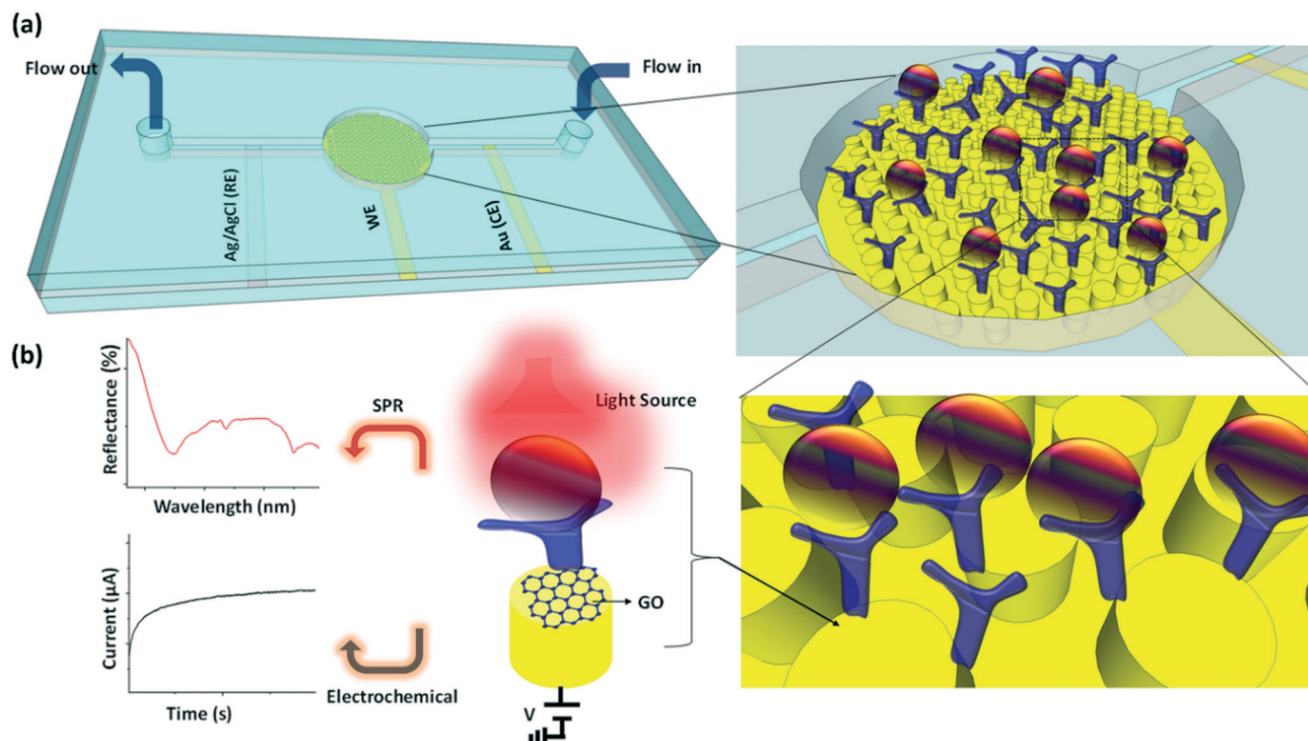


**Fig. 1** (a) Schematic representation of an integrated dual modality microfluidic sensor chip for the detection of cancer biomarkers. Zoomed-in images in (a) shows the antibody immobilization at plasmonic nanoposts *via* covalent interactions wherein  $-COOH$  groups are present at the GO–Au nanoposts that can facilitate immobilization of anti-*ErbB2* *via* forming amide bonds with  $-NH_2$  groups of anti-*ErbB2*. (b) Integrated dual-modality sensor operation showing coupling of light and voltage sources in a single nanopost to generate SPR and electrochemical signals.

enable SPR modulation<sup>42,52</sup> during kinetic binding with the target molecules. To complete the electrochemical sensor, an Au counter electrode and a silver/silver chloride (Ag/AgCl) reference electrode are placed on two sides of the nanoposts area (Fig. 2). The electrochemical measurement monitors the amperometric current flow from the nanoposts to the counter electrode under an excitation potential applied between the working and reference electrodes. In the SPR-based measurement mode, coupling of normal incident light into the nanoposts provides a reflection dip owing to the excitation of (1, 0) surface plasmon polaritons (SPPs) at the interface between the nanoposts and surrounding environment.<sup>52</sup> This integrated dual-modality sensor relies on specific immunointeractions between target breast cancer biomarker (*ErbB2*) and anti-*ErbB2* molecules on the surface of nanoposts. When the nanoposts capture *ErbB2* protein, the surface density of *ErbB2* antigen is altered. As the concentration of *ErbB2* protein varies, both the SPR wavelength and electrochemical current from the same sensing area will change, thus providing two different signatures of the specific antigen–antibody reactions.

In a typical sensor design, the pitch, diameter, and depth of the polymer nanoposts are 500 nm, 250 nm, and 210 nm, respectively. The nanoposts are sequentially coated with a 80 nm-thick Au film and a 20 nm-thick GO layer, resulting in an optical resonance at the wavelength near 699 nm when immersed in water (described later). The diameter of the round-

shaped working electrode is 3.4 mm, allowing easy alignment of the normal incident light to the sensing area. The strip-shaped Au counter and Ag/AgCl reference electrodes are 1.5 mm wide. The channels connecting to the sensing area are 400  $\mu\text{m}$  deep and 1.5 mm wide, allowing delivery of liquid samples to the sensing area.

## 2.2. Fabrication

Fabrication of the integrated dual-modality sensor involved creation of an array of polymeric nanoposts, formation of Au working and counter electrodes, formation of Ag/AgCl electrode, functionalization of GO nanosheets, covalent immobilization of anti-*ErbB2*, and formation of microfluidic channels (Fig. 2a–e).

Specifically, to form a periodic array of Au nanoposts, a silicon mold was first manufactured using standard e-beam lithography and subsequent reactive ion etching, and then was salinized for 20 min using (tridecafluoro-1,1,2,2-tetrahydrooctyl)-1-trichlorosilane. Subsequently, a hard-PDMS (h-PDMS) precursor solution was prepared by mixing poly (7–8% vinylmethyl-siloxane)-(dimethylsiloxane), (1,3,5,7-tetra vinyl-1,3,5,7-tetramethylcyclotetrasiloxane), platinum catalyst xylene and poly (25–30% methylhydro-siloxane)-(dimethylsiloxane) at the weight ratio of 3.4 : 0.1 : 0.05 : 1. Air bubbles were then removed from the mixture by degassing for 10 min. Next, the h-PDMS solution was spin-coated on the surface of the

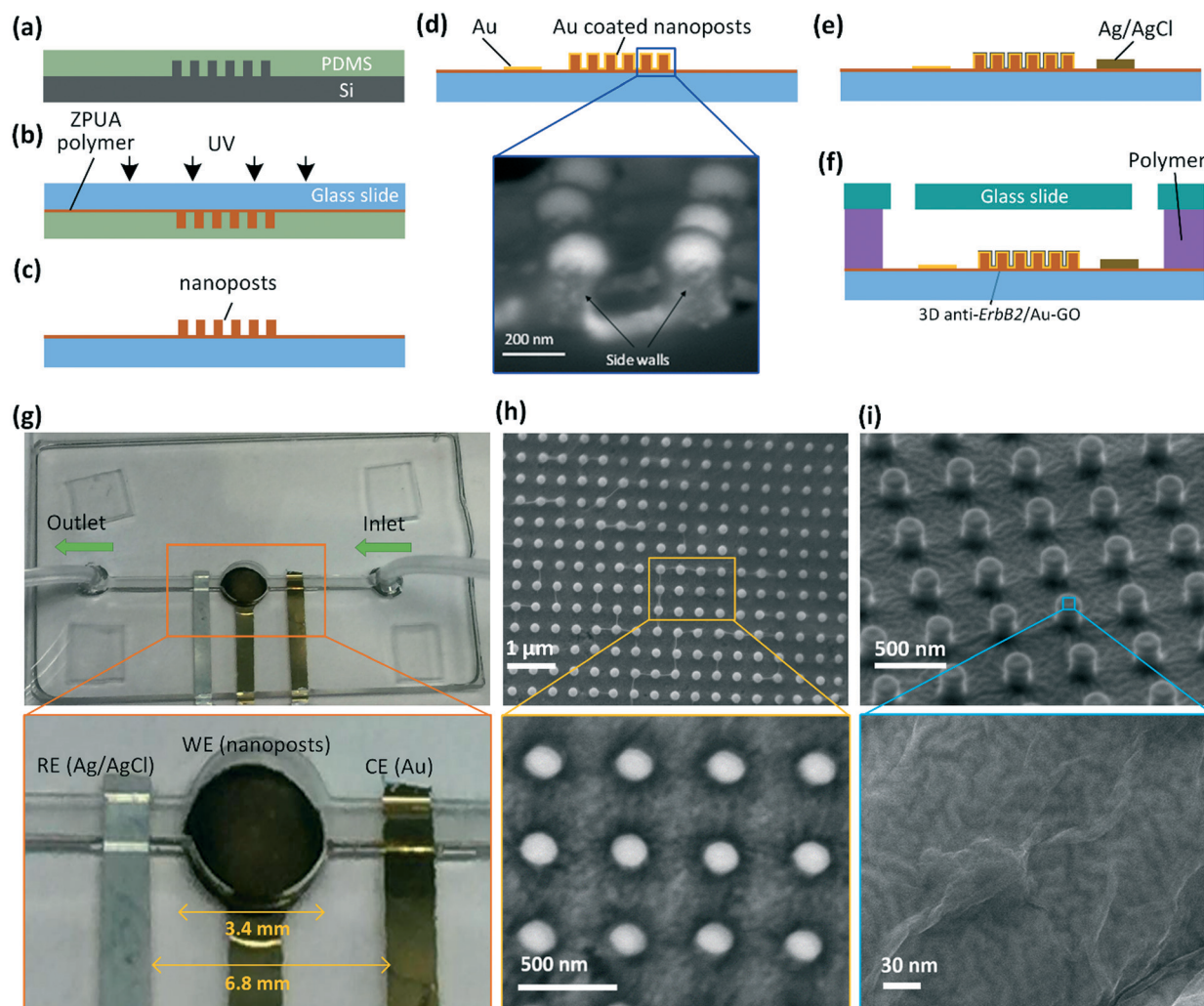


**Fig. 2** (a)–(f) Step-wise representation for the fabrication of integrated dual modality sensor. Inset of (d) shows the SEM image for the Au coating on the sidewalls of nanoposts. (g) A photograph of the fabricated integrated dual-modality sensor chip. Inset shows a zoomed-in image. (h) Top-view SEM image of the GO–Au nanoposts electrode on a glass substrate. Inset shows a zoomed-in image. (i) SEM image of fabricated 3D GO/Au plasmonic nanoposts array. Inset shows the zoomed-in top-view SEM image of a single GO/Au nanopost.

silicon mold at 1000 rpm for 40 s and cured at 70 °C for 10 min. Following that, a soft-PDMS (s-PDMS) pre-polymer solution was prepared by mixing Sylgard 184 monomer and its curing agent (Dow Corning, Midland, MI, USA) at the weight ratio of 10 : 1. After degassed for 30 min, the s-PDMS solution was poured onto the surface of the h-PDMS and cured on a hotplate at 65 °C for 2 h (Fig. 2a). Then, a PDMS-based mold, including both the s-PDMS and h-PDMS layers, was peeled off from the silicon mold. The obtained PDMS mold contains the nanoholes. It should be noted the s-PDMS pre-polymer solution was not directly poured over the silicon mold to form an s-PDMS mold since the s-PDMS pre-polymer solution has a high viscosity that makes it difficult to fully enter the nanostructures at the surface of the silicon mold. Although increasing the weight ratio of the monomer to curing agent can decrease viscosity, the cured s-PDMS are difficult to detach from the silicon mold without breaking. Compared to the s-PDMS precursor solution, the h-PDMS precursor solu-

tion has a lower viscosity and thus can conform to the nanostructured surface of the silicon mold. The formation of the additional s-PDMS layer on top of the cured h-PDMS helps when peeling the PDMS structure from the silicon mold. After the PDMS mold was formed, a drop of ultra-violet (UV) curable ZPUA precursor solution (Gelest, Inc., Morrisville, PA, USA) was dropped on the surface of the PDMS mold, and then the mold was placed on top of a glass slide. To cure ZPUA, the device was exposed to an ultraviolet light (intensity:  $3.3 \text{ mW cm}^{-2}$ ) for 5 min (Fig. 2b). Therefore, a periodic array of ZUPA nanoposts was formed on the surface of the glass slide after the PDMS mold was peeled off (Fig. 2c).

Next, a 5 nm-thick Ti layer and an 80 nm-thick Au layer were sequentially deposited onto the glass slide containing the ZPUA nanoposts array by e-beam evaporation (Fig. 2d). The samples were mounted on a tilting and rotating substrate holder to improve the sidewall Au coverage of nanoposts. The scanning electron microscopic (SEM) image (inset

of Fig. 2d) shows that the sidewalls of nanoposts were covered by Au. The round-shaped working and strip-shaped counter electrodes were patterned using a shadow mask. Similarly, a 1  $\mu\text{m}$ -thick Ag electrode was then fabricated on the same glass slide by e-beam evaporation. To form an Ag/AgCl electrode, a solution of KCl (0.1 M) was used to treat the surface of Ag electrode (Fig. 2e).

Further, the Au nanopost array was drop-coated with a 20 nm-thick layer of GO nanosheets to enable covalent conjugation of anti-*ErbB2* (Fig. 2e, h and i). In this step, a well dispersed colloidal solution of single-layer GO nanosheets (0.1 mg mL<sup>-1</sup>) was prepared in DI water *via* thorough sonication. The Au nanopost surface was next treated by oxygen plasma. As a result, the hydrophobic nature of the Au surface became hydrophilic. 20  $\mu\text{L}$  of the prepared GO suspension solution was drop cast onto the treated Au nanopost surface and dried in air at room temperature for 2 h (Fig. 2i, inset). The GO layer conformed to the shape of the nanoposts beneath it. Due to the presence of abundant functional groups (*e.g.*, -CHO, -COOH, *etc.*) at GO nanosheets, the GO layer served as an immobilization surface for covalent binding of anti-*ErbB2* molecules.

To integrate the three-electrode sensor into a microfluidic channel of photopatternable polymer,<sup>53</sup> *in situ* liquid phase polymerization process<sup>54</sup> was performed (Fig. 2, and Fig. S1, ESI<sup>†</sup>). In this step, 400  $\mu\text{m}$ -thick adhesive spacers were positioned between a 1 mm-thick glass slide and the device substrate containing all the electrodes, to form an air cavity. The glass slide contained two 1 mm-diameter through-holes (*i.e.*, the inlet and outlet of a channel) pre-drilled using a conventional milling machine with an attached 1 mm-diameter diamond drill bit. Subsequently, a photopatternable polymer solution consisting of isobornyl acrylate, crosslinker-tetraethylene glycol dimethacrylate, and photoinitiator-2,2-dimethoxy-2-phenylacetophenone at a weight ratio of 31.66 : 1.66 : 1.0 was injected into the air cavity using a plastic pipette (Fig. S1, ESI<sup>†</sup>). A photomask printed on a transparent film (6400 dpi; Finesline Imaging; Colorado Springs, CO, USA) was positioned on top of the glass slide. Next, an ultraviolet light of 12 mW cm<sup>-2</sup> intensity was used to expose the device for 60 s. To remove the unpolymerized polymer solution, the channel was washed with ethanol for 4 min. Therefore, the channel was formed and integrated with the sensor (Fig. S1, ESI<sup>†</sup>). For comparison, a control device was also manufactured and tested, which had a planar Au electrode with the same diameter as the sensor except for having no nanoposts.

### 2.3. Surface biofunctionalization

The periodic GO–Au nanoposts were functionalized with anti-*ErbB2* molecules *via* EDC–NHS coupling chemistry.<sup>55</sup> For immobilization, a solution of anti-*ErbB2* (1 mg mL<sup>-1</sup>) and EDC–NHS (EDC 0.2 M; NHS: 0.05 M) was prepared at a 1 : 1 volume ratio. A 200  $\mu\text{L}$  of this solution was injected into the channel to cover the surface of the GO–Au nanoposts. The sensor was

then kept inside a humid chamber for 12 h at 4 °C. The EDC reacted covalently with –COOH groups present at the GO nanosheets to form an intermediate *O*-acylisourea, while the NHS produced an intermediate amine-reactive stable NHS ester to allow the conjugation with primary amines of anti-*ErbB2* *via* the formation of covalent C–N bonds. A bovine serum albumin (BSA; 2 mg mL<sup>-1</sup>) solution was injected into the channel, followed by washing the sensor surface with the phosphate-buffered saline (PBS) solution (pH = 7.4) to block the non-specific sites of the sensor.<sup>56</sup>

## 3. Experimental setup and simulation

### 3.1. Chemicals

Lyophilized powder of *ErbB2* antigen (human CellExp<sup>™</sup>, fused with polyhistidine tag at the C-terminus; source: HEK293 cells and molecular weight: 72.4 kDa), *ErbB3* antigen (molecular weight: 71.5 kDa), and *ErbB4* antigen (molecular weight: 70.6 kDa, fused with 6  $\times$  histidine tag at the C-terminus) were procured from BioVision, Milpitas, CA, USA. Stock solutions of *ErbB2*, *ErbB3*, and *ErbB4* antigens were prepared using PBS (pH = 7.4), and diluted serially to form 0.1  $\mu\text{M}$  to 1.0 fM solutions. A specific polyclonal antibody of *ErbB2* was obtained from BioVision, Milpitas, CA, USA, and prepared with PBS (pH = 7.4) solution containing 1% bovine serum albumin (BSA), 30% glycerol, and 0.02% thimerosal. *N*-Ethyl-*N*-(3-dimethylaminopropyl carbodiimide) (EDC) and *N*-hydroxysuccinimide (NHS) were procured from Sigma Aldrich, MO, USA. Single layer GO nanosheets were purchased from ACS Material, Pasadena, CA, USA, wherein the elemental compositions in GO are 40.78% and 51.26% for O (wt%) and C (wt%), respectively, and the atomic ratio of C to O is 1.67. Deionized (DI) water with the resistivity of 18.2 M $\Omega$  cm was produced using a purification system from Millipore, Billerica, MA, USA, and utilized for all experiments.

### 3.2. Instruments

For electrochemical measurements, a constant potential (–0.01 V) was applied to the nanoposts-based working electrode with respect to the reference electrode. The sensor was subject to various concentrations of *ErbB2* solution in the PBS (pH = 7.4) solution mixed with an equimolar (5.0 mM) concentration of ferro/ferricyanide ([Fe(CN)<sub>6</sub>]<sup>3–/4–</sup>). All electrochemical measurements were performed using an electrochemical workstation (DY2100; Digi-Ivy, Austin, TX, US). The ferro/ferricyanide redox probe was chosen to investigate the redox activity such as radial or planar diffusion on the working electrode.

For optical measurements, a bifurcated optical fiber (BIF 400-VIS-NIR, Ocean Optics) was connected to a white light source (150 watt quartz halogen lamp; Luxtec Fiber Optics, Plainsboro NJ). A normal incident light from the source was used to illuminate the nanoposts area inside the channel through a collimator (F220SMA-A; Thorlabs, Newton, NJ). The reflected light from the sensor was collected and measured

by a UV/VIS spectrometer (USB-4000, Ocean Optics) on the other end of the bifurcated fiber.

## 4. Results and discussion

### 4.1. Electrochemical characterization

The integrated dual-modality sensor was characterized both electrochemically and optically. First, CA technique was employed to investigate electrochemical redox reactivity of the sensor. The electrochemical measurement was conducted in the PBS solution (pH = 7.4) containing a 5 mM equimolar concentration of ferro and ferricyanide ( $[\text{Fe}(\text{CN})_6]^{3-/4-}$ ) redox mediator. Fig. 3a shows that the sensor with the Au nanoparticles exhibits a 5.4-fold enhancement in output current ( $\sim 106.4 \mu\text{A}$ ) and a 3-fold reduction in response time ( $\sim 5 \text{ s}$ ), compared to those ( $\sim 19.7 \mu\text{A}$  and  $\sim 15 \text{ s}$ ) of the control device with the planar Au electrode.

To assess the benefit from using the nanoparticles on the sensor surface, the finite-element method (FEM) based soft-

ware COMSOL Multiphysics was used to study the diffusion of redox species to the nanoparticles-based and planar electrodes under an applied potential. An electroanalysis model was used,<sup>57</sup> where the geometric parameters were obtained from the SEM images of the fabricated device (Fig. 2h). The simulated concentration profile of the generated redox species near the 3D electrode indicates that the nanoparticles enable more efficient and faster diffusion of the redox species to the electrode surface, compared to the planar electrode (Fig. 3d). Therefore, the current enhancement observed in Fig. 3a is attributed to the nanoparticles that serve as vertically arranged 3D nanoelectrodes to allow the radial diffusion (Fig. 3e).<sup>19–21</sup> In contrast, the reaction at the planar electrode is controlled by linear diffusion, yielding a low redox current (Fig. 3f).

Next, the sensor was characterized using cyclic voltammetry (CV) technique in the same PBS solution (pH = 7.4) with the same redox mediator. Fig. 3b shows well-defined CV curves wherein the nanoparticles-based sensor

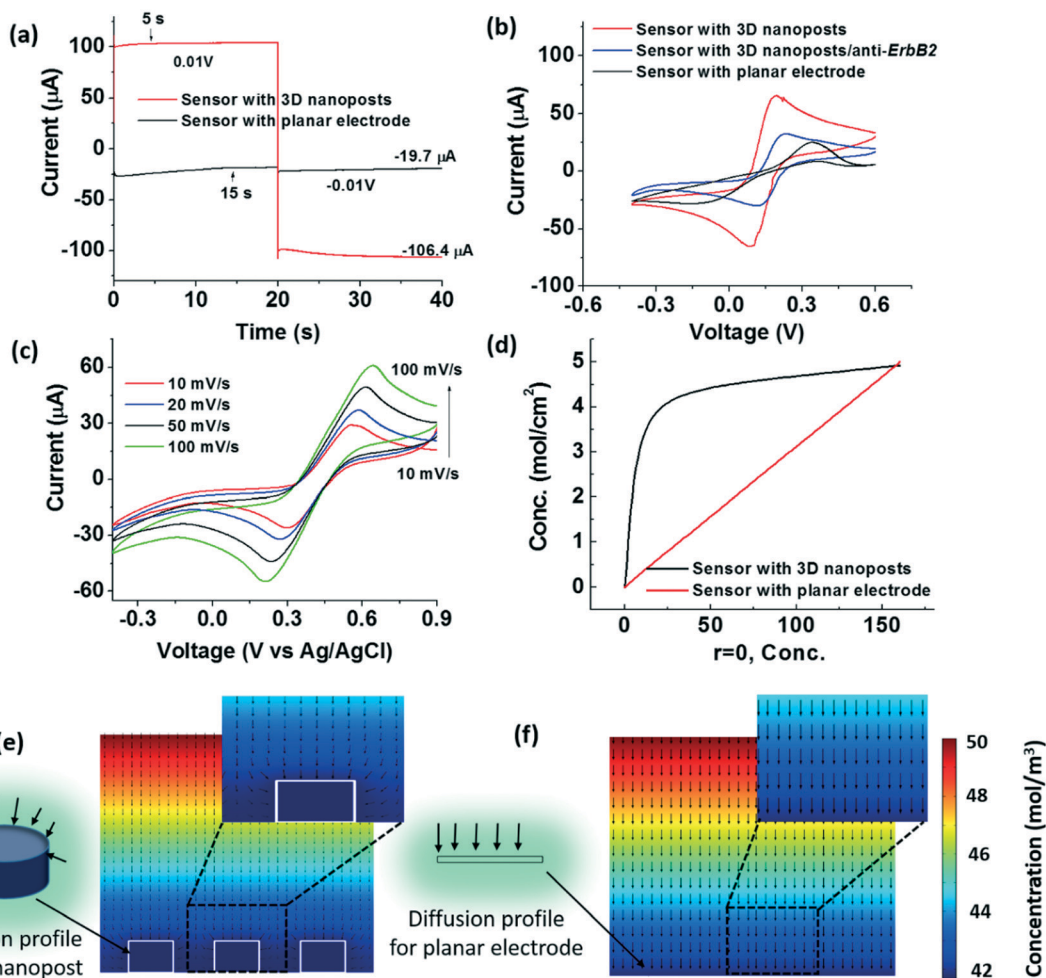


**Fig. 3** (a) CA responses of the sensor with the nanoparticles (GO–Au electrode) and without nanoparticles (planar electrode) in PBS containing a 5 mM equimolar concentration of  $[\text{Fe}(\text{CN})_6]^{3-/4-}$  redox mediator. (b) CV responses for the planar electrode, and the nanoparticles-based electrode without and with antibody. (c) CV responses of the nanoparticles-based sensor (anti-ErbB2/GO–Au) as a function of scan rate. (d) Concentration profiles of redox species diffusion near the 3D and planar electrodes. (e) and (f) Simulated diffusion profiles of redox species to the nanoparticles-based electrode (e) and the planar electrode (f).

exhibits a higher redox current than that with the planar electrode. The peak-to-peak potential difference ( $\Delta E$ ) is calculated as 0.099 V for the nanoposts-based electrode, whereas  $\Delta E$  is found as 0.452 V for the planar electrode, indicating faster electron transfer for the nanoposts.

With the immobilization of anti-*ErbB2*, the redox current of the Au nanoposts decreases due to the inherent insulating property of the antibody that slows down the electron transfer. As the scan rate increases from 10 to 100  $\text{mV s}^{-1}$ , the anodic and cathodic currents increase towards positive and negative potentials, respectively, hence, a surface-controlled diffusion process occurs on the sensor surface (Fig. 3c and S2, ESI†). According to Rendles–Sevcick equation,<sup>58</sup> the diffusion coefficient is given as:

$$D^{1/2} = \frac{i_p}{268600 \times n^{3/2} A c v^{1/2}} \quad (1)$$

where  $v^{1/2}$  is the root mean square of scan rate, and  $A$  is the area of electrode. Table 1 shows the electrochemical parameters obtained for various fabricated electrodes, including the planar electrode, and the nanoposts-based electrode with and without antibody molecules. It is found that the Au nanoposts-based electrode provides an enhanced diffusion coefficient of  $D = 3.65 \times 10^{-9} \text{ cm}^2 \text{ s}^{-1}$ , due to the radial diffusion of redox species, while the planar counterpart electrode provides a lower value of  $D = 0.51 \times 10^{-9} \text{ cm}^2 \text{ s}^{-1}$ . The heterogeneous electron transfer rate constant ( $k_s$ ) is obtained based on Laviron's theory.<sup>52</sup> The Au nanoposts-based electrode provides  $k_s = 0.79 \text{ cm s}^{-1}$ , which is about 3.3 times of magnitude greater than the planar electrode ( $k_s = 0.24 \text{ cm s}^{-1}$ ).

## 4.2. SPR characterization

Under a normal incident light, SPR is generated at the interface between the Au nanoposts and surrounding environment. For a two-dimensional structure with square lattice,<sup>52</sup> the free-space wavelength of incident light to excite SPPs is given as:

$$\lambda = \frac{\Lambda}{\sqrt{i^2 + j^2}} \sqrt{\frac{\epsilon_{\text{Au}} \epsilon_d}{\epsilon_{\text{Au}} + \epsilon_d}} \quad (2)$$

where  $\epsilon_d$  and  $\epsilon_{\text{Au}}$  are the dielectric constants of the surrounding medium and Au, respectively,  $\Lambda$  is the lattice constant, and  $(i, j)$  corresponds to the order of SPPs. The bulk index sensitivity of this Au nanoposts array was measured to be

449.6 nm per refractive index unit (nm per RIU) by introducing water (refractive index: 1.33), acetone (1.363), ethanol (1.365), isopropyl alcohol (1.377), and chloroform (1.44) onto the sensor surface (Fig. 4a). Fig. 4b compares the changes in reflectance spectra for the Au nanoposts with and without GO coating, and after anti-*ErbB2* immobilized on the GO–Au surface. Before the GO coating, the spectrum exhibits a reflection dip associated with (1, 0) SPP at 549 nm in air, as confirmed from the simulated spectrum (denoted as dip I in Fig. 4c) and electric field distributions (dip I in Fig. 4d), where the standing wave feature above the Au nanoposts indicates the excitation of SPPs. A redshift of 17.7 nm in air was observed with the GO coating on the Au nanoposts due to the increase in local refractive index (Fig. 4b). When the Au/GO nanoposts are exposed to the PBS solution with anti-*ErbB2* molecules, a narrow resonance dip appears at 699 nm. To better understand the resonance mode used in the SPR measurement, we conducted the FEM simulation using the COMSOL multiphysics software. In this simulation, periodic boundary conditions were applied at the boundaries in parallel with the light propagation direction. The top and bottom of the computation regions were placed with two perfectly matched layers (PMLs) so that all the scattered electromagnetic waves from the nanopost arrays were absorbed at the PMLs.<sup>52</sup> In addition, the refractive index of the PMLs was set to the same value of neighbouring media to simulate an infinitely thick substrate.<sup>52</sup> The simulated spectrum for the Au nanoposts without GO in water presents a new resonance dip (denoted as dip II in Fig. 4c) near 700 nm wherein the electric field distribution confirms the excitation of SPPs at the interface between water and the Au nanoposts (Fig. 4d).

## 4.3. Electrochemical detection of biomarker

The sensor was exploited to detect specific concentrations of biomarker (*ErbB2* antigen) using the CA measurement method. The GO–Au nanoposts functionalized with anti-*ErbB2* were exposed to different concentrations of *ErbB2* antigen ranging from 1.0 fM to 0.1  $\mu\text{M}$  by injecting corresponding analyte solutions into the microfluidic channel. Fig. 5a and b show the CA responses to different *ErbB2* concentrations for a sensing potential of 0.01 V with and without the nanoposts, respectively. The CA responses are found to saturate at a constant current within 5 s (Fig. 5a). The transient responses (Fig. 5a) show a larger steady-state current owing to the radial diffusion occurring at the surface of nanoposts compared to the current at the planar electrode surface (Fig. 5b). In both the cases, the current decreases with

**Table 1** Electrochemical parameters for various working electrodes

Electrodes	Peak current ( $\mu\text{A}$ )	Peak-to-peak potential difference (V)	Diffusion coefficient ( $\text{cm}^2 \text{ s}^{-1}$ )	Heterogeneous electron transfer rate constant ( $k_s$ ; $\text{cm s}^{-1}$ )
Planar Au–GO electrode	24.6	0.452	$0.51 \times 10^{-9}$	0.24
Nanoposts-based Au–GO electrode	65.2	0.099	$3.65 \times 10^{-9}$	0.79
Nanoposts-based Au–GO electrode with anti- <i>ErbB2</i>	32.5	0.104	$0.88 \times 10^{-9}$	0.51

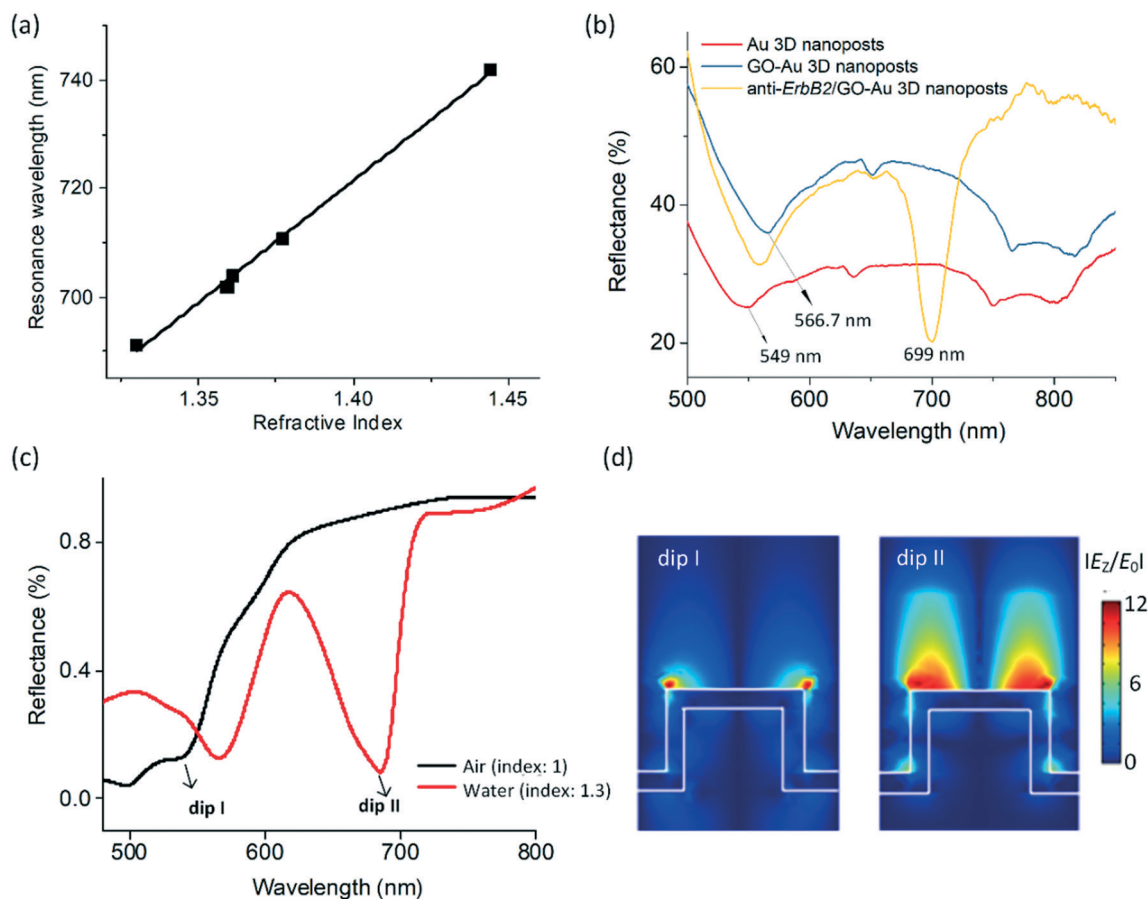


**Fig. 4** (a) Bulk refractive index sensitivity of the plasmonic crystal in presence of various index materials. (b) SPR responses showing a redshift of 17.7 nm in air after coating the Au nanoposts with GO. After anti-*ErbB2* immobilization on GO-Au nanoposts, the resonance is redshifted to 699 nm. (c) Simulated reflectance spectra of the plasmonic nanostructures without GO in air (refractive index: 1) and water (refractive index: 1.3). The SPR resonances are denoted as dip I and II. (d) Simulated cross-sectional electric field distributions at the resonances (dip I and II) in (c).

increasing *ErbB2* concentrations. This is due to the insulating layer of immunocomplex formation *via* binding of specific sites such as epitope at anti-*ErbB2* and paratopes at *ErbB2* antigen which can obstruct the acceleration of the electrons generated from redox reaction. As the number of *ErbB2* antigen molecules bound to the sensor surface increases, the thickness of the resulting immunocomplex layer increases, leading to reduction in output currents. The calibration plots in Fig. 5c show that the sensor current is inversely proportional to the logarithmic concentration of *ErbB2* antigen. Approximately, a five-fold enhancement was obtained for the sensitivity ( $20.47 \mu\text{A } \mu\text{M}^{-1} \text{cm}^{-2}$ ) of the nanoposts-based sensor compared to that of the control sensor without using any nanoposts ( $3.94 \mu\text{A } \mu\text{M}^{-1} \text{cm}^{-2}$ ), owing to the larger surface area and the radial diffusion of redox species. The larger surface area of the nanoposts enhances the loading capacity of GO nanosheets as well as antibody molecules, leading to an increased higher affinity towards *ErbB2*.

For the selectivity measurements, the sensor with the nanoposts was exposed to the non-specific interfering antigen species *ErbB3* and *ErbB4* in the *ErbB* receptor tyrosine kinase family. Similarly, the CA method was employed to measure the response of the sensor (Fig. 5d). When *ErbB2*

antigen ( $0.1 \mu\text{M}$ ) was added to nonspecific *ErbB3* ( $0.1 \mu\text{M}$ ) alone, *ErbB4* ( $0.1 \mu\text{M}$ ) alone, and a mixture of *ErbB3* ( $0.1 \mu\text{M}$ ) and *ErbB4* ( $0.1 \mu\text{M}$ ), the sensor response did not change significantly as is evident from its low relative standard deviation (RSD;  $\pm 1.1\%$ ) from the initial response with *ErbB2* ( $0.1 \mu\text{M}$ ) only, indicating a good selectivity due to incorporating anti-*ErbB2* on the sensor surface.

The sensor was further examined for reproducibility with four identical sensors using the CA technique in presence of  $1.0 \text{ fM}$  concentration of *ErbB2*. This sensor shows a high reproducibility with a minute deviation (RSD:  $\pm 1.95\%$ ) (Fig. 5e). The obtained high reproducibility of the sensor may be due to the high periodicity and uniform assembly of the Au nanoposts. In addition, the stability test for the nanoposts-based sensor was conducted once a week over a four-week period. For each measurement, the sensor was washed with the PBS solution to remove unbound molecules from the sensor surface. When not in use, the sensor was stored at  $4 \text{ }^\circ\text{C}$  to avoid denature of antibody on the sensor surface. Overall, this sensor exhibited a stable amperometric signature (Fig. 5f), although after three weeks, a  $1.2 \pm 0.3\%$  reduction in output current was found.

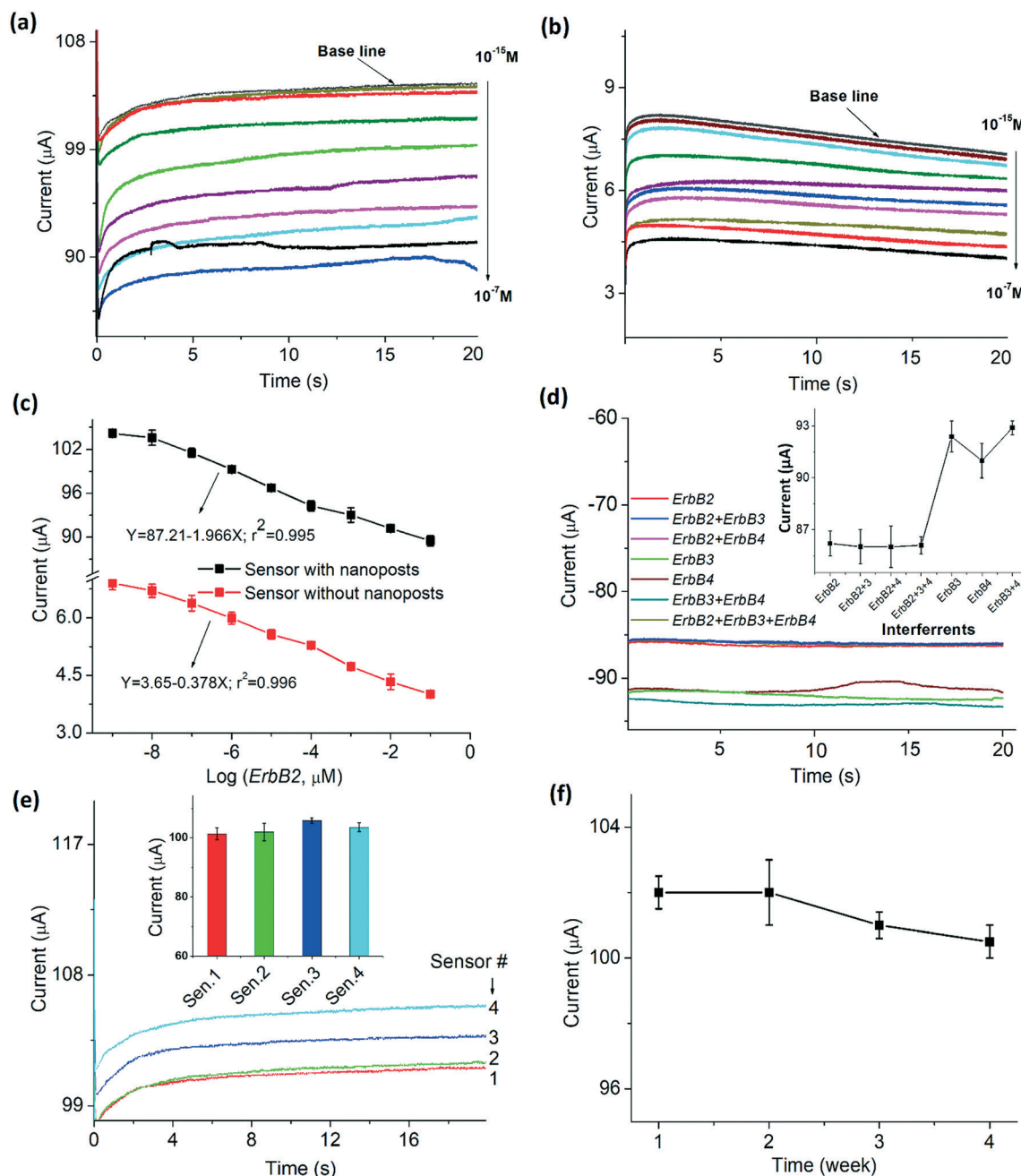


**Fig. 5** Sensing responses for the sensors with and without incorporating nanoparticles. The measurements were conducted as a function of *ErbB2* concentration at a constant sensing potential of 0.01 V in presence of PBS (pH 7.4) containing 5 mM  $[\text{Fe}(\text{CN})_6]^{3-/4-}$ . (a) CA responses for the sensor with the nanoparticles. (b) CA responses for the sensor with the planar Au electrode. (c) Calibration plots for both the sensor responses in (a) and (b). Error bars represent three repeated measurements of the sensor. (d) Selectivity test of the sensor in presence of specific *ErbB2* (0.1  $\mu\text{M}$ ) and nonspecific *ErbB3* (0.1  $\mu\text{M}$ ) and *ErbB4* (0.1  $\mu\text{M}$ ). Inset shows the current responses versus several interferences. (e) Reproducibility test of the sensor conducted with four identical sensors at 1.0 fM concentration of *ErbB2*. Error bar on each data point represents the standard deviation of five measurements. (f) Stability test of the sensor performed for four weeks. Error bars represent the standard deviations obtained using four identical sensors that respond to 1.0 fM concentration of *ErbB2* biomarker once a week over a four-week period.

#### 4.4. SPR detection of biomarker

In addition to the electrochemical sensing, the microfluidic sensor was used to conduct the SPR-based detection of *ErbB2* antigen biomarker. It was found that when the *ErbB2* concentrations were lower than 10 pM, the resonance wavelength of the sensor was almost insensitive to changes in *ErbB2* con-

centration. This is because the resulting refractive index variation was too small to be detected by this plasmonic sensor. At plasmonic resonances, optical energy dissipations in Au result in a low Q-factor of resonances, thus restricting the sensitivity of the sensor. Fig. 6a shows the SPR spectra of this sensor as a function of *ErbB2* concentration ranging from 10

pM to 0.1  $\mu\text{M}$  in the PBS solution (pH = 7.4). A reflection dip was found at the resonance wavelength of 701.6 nm with 10 pM *ErbB2* concentration when the anti-*ErbB2* conjugated nanoposts array was excited by the normal incident light. As the *ErbB2* concentration increased from 10 pM to 0.1 nM, 1 nM, 10 nM and 0.1  $\mu\text{M}$ , the resonance wavelength of the sensor redshifted from 701.6 nm to 703.1 nm, 704.3 nm, 705.2 nm and 705.9 nm, respectively.

The sensor surface was cleaned with the PBS solution before introducing a new analyte solution on the sensor surface. Fig. 6b shows the calibration plot of the sensor between the logarithmic *ErbB2* concentrations and the SPR resonance wavelengths. The resonance shifted towards higher wavelengths with increasing concentration, resulting from the specific binding of *ErbB2* molecules increasing the refractive index at the sensor surface. This sensor shows a sensitivity of  $1.35 \text{ nm } \mu\text{M}^{-1}$  within the concentration range of *ErbB2* from 10 pM to 1 nM and a sensitivity of  $0.80 \text{ nm } \mu\text{M}^{-1}$  within the concentration range of *ErbB2* from 1 nM to 0.1  $\mu\text{M}$ .

The stability test for the SPR measurement was conducted once every week over a four-week period (Fig. 6c). During each measurement, the sensor was exposed to 1 nM *ErbB2* concentration and the obtained resonance wavelength was recorded. After the test, the sensor surface was washed by flowing the PBS solution (pH = 7.4) into the channel and then was stored at 4  $^{\circ}\text{C}$  until next test. The result shows that after four weeks, the resonance wavelength for 1 nM *ErbB2* concentration exhibited a minor shift of about 0.35 nm towards shorter wavelengths, compared to that obtained initially (704.4 nm resonance wavelength), which may be caused by denaturation of immobilized anti-*ErbB2* molecules.

Fig. 6d demonstrates the ability of the sensor to optically track binding kinetics of antigen-antibody interactions at the sensor surface as the *ErbB2* concentration increased from 10 pM to 0.1 nM, 1 nM, 10 nM and 0.1  $\mu\text{M}$  in the PBS solution (pH = 7.4) with the same redox mediator. The sensor surface was first covered by the PBS solution, and then, the *ErbB2* (10 pM) solution flowed into the channel. This association phase induced a redshift of 0.7 nm. As the *ErbB2*

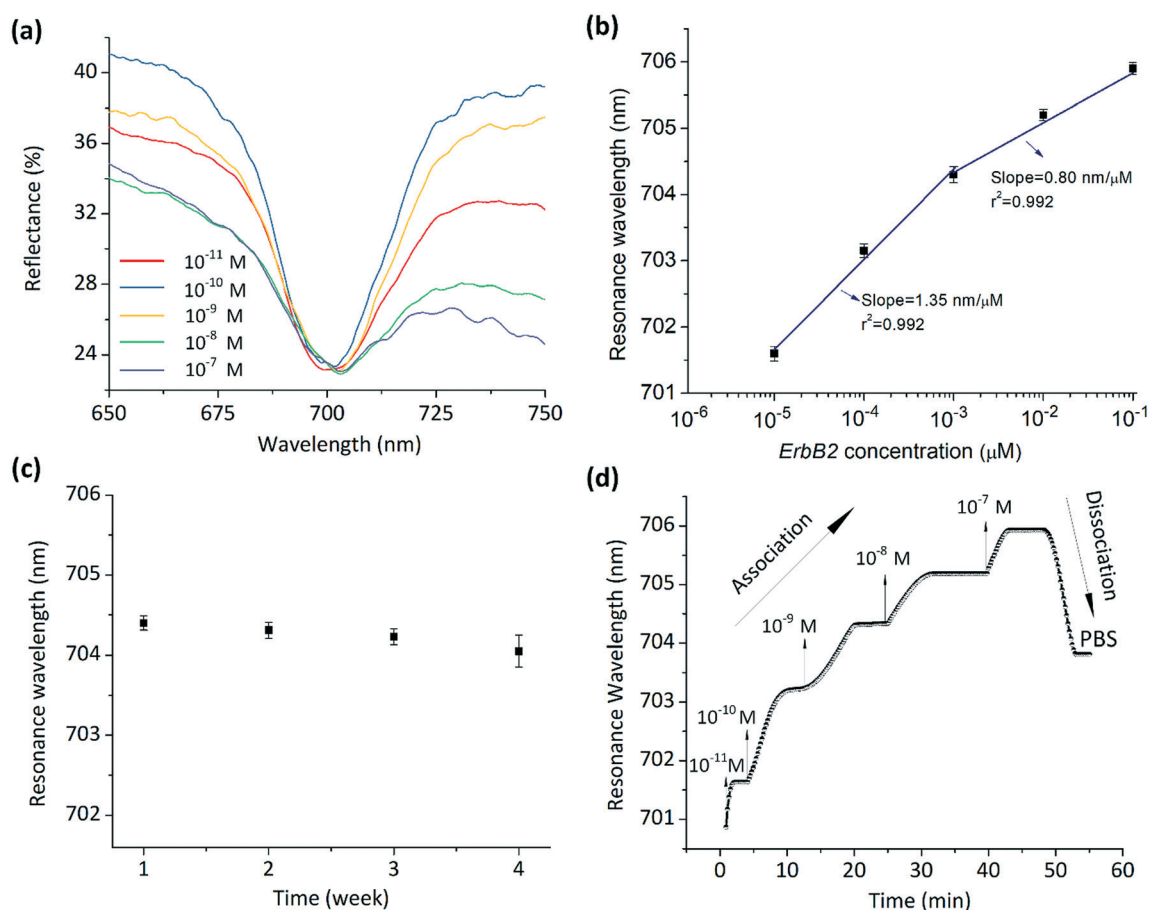


**Fig. 6** (a) Full SPR spectra of the GO coated Au nanopost array by varying the *ErbB2* concentration from  $1 \times 10^{-11} \text{ M}$  to  $1 \times 10^{-7} \text{ M}$ . (b) SPR resonance wavelengths as a function of *ErbB2* concentrations. Error bars represent the standard deviations obtained using five independent measurements. (c) Stability test of the sensor at 1 nM *ErbB2* concentration over four weeks, showing the resonance wavelength of the sensor as a function of time. Error bars represent the standard deviations obtained using four identical sensors that respond to 1 nM concentration of *ErbB2* biomarker once a week over a four-week period. (d) Transient response for the detection of *ErbB2* molecules at the concentrations of 10 pM, 0.1 nM, 1 nM, 10 nM and 0.1  $\mu\text{M}$ , showing the association and dissociation phases for antigen-antibody interactions in the PBS (pH = 7.4) solution.

concentration increased from 10 pM to 0.1 nM, this sensor provided a redshift of 1.5 nm in the association phase. When the *ErbB2* concentration further increased to 1 nM, 10 nM and 0.1  $\mu\text{M}$ , the resonance redshifted by 1.2 nm, 0.9 nm, and 0.7 nm, respectively. In the dissociation phase, the sensor was washed with the PBS solution to remove the loosely bound *ErbB2* molecules from the surface of the nanoposts, resulting in shifting the resonance wavelength to 703.8 nm.

Using the Hill equation,<sup>59</sup> the association ( $K_a$ ) and dissociation ( $K_d$ ) constants for the *ErbB2* antigen and anti-*ErbB2* immunocomplex have been calculated. The  $K_a$  and  $K_d$  of antibody and antigen can be expressed as  $n\text{Ag} + \text{Ab} \xrightleftharpoons{K_d} \text{Ag}_n\text{Ab}$ ,

where  $n$  is known as the Hill coefficient,  $\text{Ag}$  is *ErbB2* captured by the sensor and  $\text{Ab}$  is anti-*ErbB2* immobilized on nanoposts surface. The equilibrium constant  $K_d$  is given by  $K_d = [\text{Ag}]^n[\text{Ab}]/[\text{Ag}_n\text{Ab}]$ , where  $K_d$  is the reciprocal of  $K_a$ , and  $n$  can be estimated using the Hill plot. The Hill plot is the curve between  $\log \theta$  and  $\log(\text{ErbB2})$  and  $\theta$  is given by  $\theta = Y/(1 - Y)$ , a ratio of the amount of bound *ErbB2* to the amount of immobilized anti-*ErbB2* and  $Y$  is the ratio of the change of wavelength and maximum wavelength. The values of  $K_d$ ,  $K_a$  and  $n$  are found as  $0.472 \times 10^{-6}$  M,  $2.11 \times 10^6$  M, and 0.207, respectively. With  $n$  (0.207) < 1, *i.e.* the cooperativity is negative. When the *ErbB2* molecule binds to specific anti-*ErbB2*, the affinity of this anti-*ErbB2* to non-specific species declines. The higher association constant of anti-*ErbB2* conjugated nanoposts indicates a higher affinity towards specific *ErbB2* antigen.

#### 4.5. Simultaneous measurements using dual modalities

We conducted both the electrochemical and SPR measurements simultaneously using the dual-modality sensor in the presence of 10 nM concentration of *ErbB2* molecules. As shown in Fig. 7, the electrochemical measurement shows a reduction in chronoamperometric current from 105  $\mu\text{A}$  (*i.e.*, the baseline current) to 88.5  $\mu\text{A}$ . Based on the electrochemical calibration curve (Fig. 5c), the *ErbB2* concentration obtained using the electrochemical measurement is  $10.1 \pm 0.4$  nM (mean  $\pm$  standard deviation for 5 measurements), which agrees well with the known concentration of 10 nM. At the same time, the SPR measurement shows that the resonance wavelength of the sensor redshifts from 699 nm (*i.e.*, the baseline wavelength) to 705.2 nm. Correspondingly, based on the SPR calibration curve (Fig. 6b), the obtained *ErbB2* concentration is  $10.2 \pm 0.3$  nM (mean  $\pm$  standard deviation for 5 measurements). Therefore, the electrochemical and SPR measurements using the single sensor provide almost consistent results for the detection of *ErbB2* molecules when the *ErbB2* concentration under measurement falls in the common dynamic range of both the methods. It should be noted that in the optical measurement, we utilized a broadband light source with the total input light intensity of 20  $\text{W cm}^{-2}$  over the wavelength range from 500 nm to 750 nm. The light intensity at the central resonance wavelength of 699 nm with a bandwidth of  $\sim 39$  nm was only  $\sim 18\%$  of the total in-

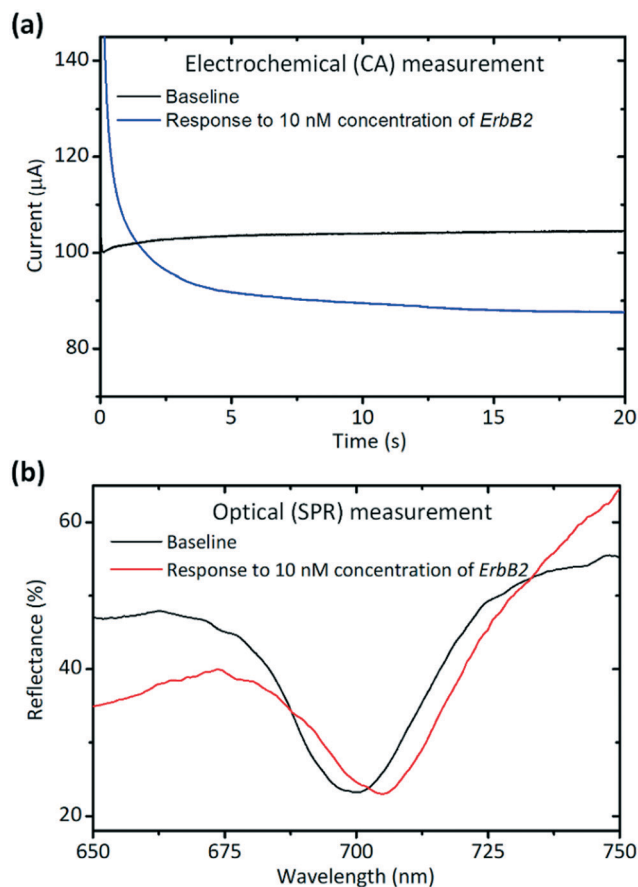


Fig. 7 Simultaneous measurements using the CA-based electrochemical (a) and SPR-based optical (b) methods on the single dual-modality sensor. The sensor was exposed to 10 nM concentration of *ErbB2* molecules.

put intensity. Because the maximum field intensity enhancement factor is  $12 \times 12 = 144$  (where 12 is the factor by which the electric field enhancement occurs at the resonance at the sensor surface as compared to the input field amplitude; see Fig. 4d), it is estimated that the local light intensity at the resonance structures is  $\sim 18\% \times 20 \text{ W cm}^{-2} \times 144 = \sim 518 \text{ W cm}^{-2}$ , which is too low to result in thermophoresis or photophoresis at the sensor surface.<sup>60</sup>

#### 4.6. Comparison with state-of-art sensors

Tables 2 and 3 compare the performance of this sensor with many reported sensors for the detection of *ErbB2* biomarker. Compared to the electrochemical sensors using graphene foam-TiO<sub>2</sub>,<sup>56</sup> Au nanoparticles,<sup>61</sup> and GO-SiO<sub>2</sub> nanoparticles,<sup>17</sup> and the optical sensors using microrings,<sup>62</sup> 1D distributed feedback grating<sup>44</sup> the present integrated dual-modality sensor offers a competitive detection range of 1.0 fM–0.1  $\mu\text{M}$ , and a high sensitivity of  $20.47 \mu\text{A } \mu\text{M}^{-1} \text{ cm}^{-2}$  for the electrochemical detection (Table 2), and a sensitivity of  $1.35 \text{ nm } \mu\text{M}^{-1}$  in the concentration range of 10 pM–1 nM, a sensitivity of  $0.80 \text{ nm } \mu\text{M}^{-1}$  in the concentration range of 1 nM–0.1  $\mu\text{M}$  for the SPR detection (Table 3) of *ErbB2*.

**Table 2** Comparison of the performance of our electrochemical sensor with that of other electrochemical immunosensors for the detection of *ErbB2* biomarker

Electrochemical working electrodes	Measurement methods	Sensitivity	Dynamic range (pM)	Limit of detection (pM)	Ref.
Au nanoparticles	Electrochemical (voltammetry)	2.2 $\mu\text{A pM}^{-1} \text{cm}^{-2}$	$7.25 \times 10^{-4}$ –72.5	$2.68 \times 10^{-4}$	61
Graphene foam-TiO <sub>2</sub>	Electrochemical (voltammetry)	0.585 $\mu\text{A } \mu\text{M}^{-1} \text{cm}^{-2}$	0.001– $1.0 \times 10^5$	0.001	56
Graphene oxide-SiO <sub>2</sub> nanoparticles	Electrochemical (impedance)	NA	$1$ – $1 \times 10^6$	1.0	17
Functionalized ZnO nanofibers	Electrochemical (impedance)	7.76 $\text{k}\Omega \mu\text{M}^{-1} \text{cm}^{-2}$	0.001– $5.0 \times 10^5$	0.001	63
Cysteamine-AuNPs	Electrochemical (impedance)	3.83 $\text{k}\Omega \text{pM}^{-1}$	0.0072– $7.2 \times 10^3$	0.0024	64
Au-GO nanoposts	Electrochemical (amperometry)	20.47 $\mu\text{A } \mu\text{M}^{-1} \text{cm}^{-2}$	0.001– $1 \times 10^5$	0.001	This work

**Table 3** Comparison of the performance of our SPR sensor with that of other optical immunosensors for the detection of *ErbB2* biomarker

Optical resonators	Measurement methods	Sensitivity ( $\text{nm } \mu\text{M}^{-1}$ )	Dynamic range (pM)	Limit of detection (pM)	Ref.
Optofluidic ring resonator	Whispering gallery mode	74.2	94–240	72	62
		27.4	362–725		
1D distributed feedback grating	First-order diffraction mode	4.6	$75$ – $5.4 \times 10^4$	75	44
Au-GO nanoposts	SPR mode	1.35	$10$ – $1 \times 10^3$	10	This work
		0.8	$1 \times 10^3$ – $1 \times 10^5$		

The present integrated dual-modality sensor incorporates both electrochemical and SPR detection methods on a single nanopatterned substrate for recognizing and quantifying *ErbB2* breast cancer biomarker, offering many novelties:

- The integrated dual-modality design potentially will help increase detection reliability, due to the ability of the sensor to generate two readouts for a specific antigen–antibody reaction at the sensor surface.

- The electrochemical detection mode of the sensor benefits from the presence of the lithographically formed nanoposts on the surface of the working electrode, enabling efficient radial diffusion of redox species. This provides a fM-level limit of detection (LOD) for quantifying *ErbB2* biomarker using the electrochemical mode, which will be clinically important to early-stage cancer diagnosis.

- While the SPR detection mode has a higher LOD (on the order of 10 pM for *ErbB2*), it enables dynamic tracking of antigen–antibody interactions at the same surface where the electrochemical detection takes place. The ability to track association and dissociation processes will potentially help scientists to better understand molecular recognition behaviors for optimizing a target antibody for a specific antigen.

- Further, from a sample consumption perspective, the required sample volume used in the presented integrated dual-modality sensor is less than that used in two spatially separated electrochemical and SPR sensors.

## 5. Conclusions

To summarize, an integrated dual-modality sensor integrating electrochemical and SPR measurements was developed for the detection of a breast cancer biomarker. The substrate for SPR detection consists of an array of periodically arranged Au nanoposts functionalized with GO nanosheets and antibody (anti-*ErbB2*), while the same Au nanoposts also serve as

a working electrode of the integrated electrochemical sensor. In addition to increasing the surface area and loading capability for the immobilized anti-*ErbB2* molecules, these nanoposts enable SPR, and also serve as the vertical nanoelectrodes enabling the radial diffusion of redox species onto the sensor surface. The sensor with the nanoposts exhibits 5.4-fold enhancement in output current and a 3-fold reduction in response time, compared to the counterpart device with the planar electrode. The SPR detection mode allows a dynamic tracking of the associations and dissociations of biomarker molecules, which is generally a limitation of an electrochemical sensor. Unlike the nanoparticles, nanotubes, and nanowires-based sensors, this integrated dual-modality sensor offers an excellent reproducibility due to the ordered and uniform nanostructures.

## Conflicts of interest

There are no conflicts to declare.

## Acknowledgements

This work was supported in part by the Iowa State University's Plant Sciences Institute, and in part by the National Science Foundation under Grants ECCS-0954765, ECCS-1711839, CCF-1331390, and IIP-1602089. The authors thank the Microelectronics Research Center at the Iowa State University, Ames, IA, and the Minnesota Nano Center at the University of Minnesota, Twin Cities, MN, for manufacturing facilities.

## Notes and references

- 1 Y. Hu, D. H. Fine, E. Tasciotti, A. Bouamrani and M. Ferrari, Nanodevices in diagnostics, *Wiley Interdiscip. Rev.: Nanomed. Nanobiotechnol.*, 2011, 3, 11–32.

- 2 A. Jemal, R. Siegel, E. Ward, Y. Hao, J. Xu, T. Murray and M. J. Thun, Cancer statistics, *Ca-Cancer J. Clin.*, 2008, **58**, 71–96.
- 3 A. Powers and S. Palecek, Protein analytical assays for diagnosing, monitoring, and choosing treatment for cancer patients, *J. Healthc. Eng.*, 2012, **3**, 503–534.
- 4 A. S. Gauchez, N. Ravel, D. Villemain, F. X. Brand, D. Pasquier, R. Payan and M. Mousseau, Evaluation of a manual ELISA kit for determination of HER2/neu in serum of breast cancer patients, *Anticancer Res.*, 2008, **28**, 3067–3073.
- 5 R. Malhotra, V. Patel, B. V. Chikkaveeraiah, B. S. Munge, S. C. Cheong, R. B. Zain, M. T. Abraham, D. K. Dey, J. S. Gutkind and J. F. Rusling, Ultrasensitive detection of cancer biomarkers in the clinic by use of a nanostructured microfluidic array, *Anal. Chem.*, 2012, **84**, 6249–6255.
- 6 M. Hu, J. Yan, Y. He, H. Lu, L. Weng, S. Song, C. Fan and L. Wang, Ultrasensitive, multiplexed detection of cancer biomarkers directly in serum by using a quantum dot-based microfluidic protein chip, *ACS Nano*, 2009, **4**, 488–494.
- 7 J. Richard, C. Sainsbury, G. Needham, J. Farndon, A. Malcolm and A. Harris, Epidermal-growth-factor receptor status as predictor of early recurrence of and death from breast cancer, *Lancet*, 1987, **329**, 1398–1402.
- 8 J. R. Sainsbury, G. V. Sherbet, J. R. Farndon and A. L. Harris, Epidermal-growth-factor receptors and oestrogen receptors in human breast cancer, *Lancet*, 1985, **325**, 364–366.
- 9 H. Zhang, A. Berezov, Q. Wang, G. Zhang, J. Drebin, R. Murali and M. I. Greene, ErbB receptors: from oncogenes to targeted cancer therapies, *J. Clin. Invest.*, 2007, **117**, 2051–2058.
- 10 N. Iqbal and N. Iqbal, Human epidermal growth factor receptor 2 (HER2) in cancers: overexpression and therapeutic implications, *Mol. Biol. Int.*, 2014, **2014**, 490308.
- 11 B. M. Venkatesan and R. Bashir, Nanopore sensors for nucleic acid analysis, *Nat. Nanotechnol.*, 2011, **6**, 615–624.
- 12 E. Stern, A. Vacic, N. K. Rajan, J. M. Criscione, J. Park, B. R. Ilic, D. J. Mooney, M. A. Reed and T. M. Fahmy, Label-free biomarker detection from whole blood, *Nat. Nanotechnol.*, 2010, **5**, 138–142.
- 13 F. Eftekhari, C. Escobedo, J. Ferreira, X. Duan, E. M. Girotto, A. G. Brolo, R. Gordon and D. Sinton, Nanoholes as nanochannels: flow-through plasmonic sensing, *Anal. Chem.*, 2009, **81**, 4308–4311.
- 14 M. E. Stewart, C. R. Anderton, L. B. Thompson, J. Maria, S. K. Gray, J. A. Rogers and R. G. Nuzzo, Nanostructured plasmonic sensors, *Chem. Rev.*, 2008, **108**, 494–521.
- 15 D. A. Heller, H. Jin, B. M. Martinez, D. Patel, B. M. Miller, T. K. Yeung, P. V. Jena, C. Höbartner, T. Ha, S. K. Silverman and M. S. Strano, Multimodal optical sensing and analyte specificity using single-walled carbon nanotubes, *Nat. Nanotechnol.*, 2009, **4**, 114–120.
- 16 A. V. Kondrashina, R. I. Dmitriev, S. M. Borisov, I. Klimant, I. O'Brien, Y. M. Nolan, A. V. Zhdanov and D. B. Papkovsky, A phosphorescent nanoparticle-based probe for sensing and imaging of (intra) cellular oxygen in multiple detection modalities, *Adv. Funct. Mater.*, 2012, **22**, 4931–4939.
- 17 S. Myung, A. Solanki, C. Kim, J. Park, K. S. Kim and K. B. Lee, Graphene-encapsulated nanoparticle-based biosensor for the selective detection of cancer biomarkers, *Adv. Mater.*, 2011, **23**, 2221–2225.
- 18 G. Zheng, F. Patolsky, Y. Cui, W. U. Wang and C. M. Lieber, Multiplexed electrical detection of cancer markers with nanowire sensor arrays, *Nat. Biotechnol.*, 2005, **23**, 1294–1301.
- 19 J. Heinze, Ultramicroelectrodes in electrochemistry, *Angew. Chem., Int. Ed. Engl.*, 1993, **32**, 1268–1288.
- 20 R. J. Forster, Microelectrodes: new dimensions in electrochemistry, *Chem. Soc. Rev.*, 1994, **23**, 289–297.
- 21 M. E. Sandison and J. M. Cooper, Nanofabrication of electrode arrays by electron-beam and nanoimprint lithographies, *Lab Chip*, 2006, **6**, 1020–1025.
- 22 L. M. Lu, H. B. Li, F. Qu, X. B. Zhang, G. L. Shen and R. Q. Yu, In situ synthesis of palladium nanoparticle–graphene nanohybrids and their application in nonenzymatic glucose biosensors, *Biosens. Bioelectron.*, 2011, **26**, 3500–3504.
- 23 X. Li, C. Zhao and X. Liu, A paper-based microfluidic biosensor integrating zinc oxide nanowires for electrochemical glucose detection, *Microsyst. Nanoeng.*, 2015, **9**, 1–7.
- 24 D. Vilela, J. Garoz, A. Colina, M. C. González and A. Escarpa, Carbon nanotubes press-transferred on PMMA substrates as exclusive transducers for electrochemical microfluidic sensing, *Anal. Chem.*, 2012, **84**, 10838–10844.
- 25 K. Mondal, Md. A. Ali, V. V. Agrawal, B. D. Malhotra and A. Sharma, Highly sensitive biofunctionalized mesoporous electrospun TiO<sub>2</sub> nanofiber based interface for biosensing, *ACS Appl. Mater. Interfaces*, 2014, **6**, 2516–2527.
- 26 L. Yang and L. Dong, Selective nanofiber deposition using a microfluidic confinement approach, *Langmuir*, 2010, **26**, 1539–1543.
- 27 W. C. Law, K. T. Yong, A. Baev and P. N. Prasad, Sensitivity improved surface plasmon resonance biosensor for cancer biomarker detection based on plasmonic enhancement, *ACS Nano*, 2011, **5**, 4858–4864.
- 28 M. Brigham-Burke, J. R. Edwards and D. J. O'Shannessy, Detection of receptor-ligand interactions using surface plasmon resonance: model studies employing the HIV-1 gp120/CD4 interaction, *Anal. Biochem.*, 1992, **205**, 125–131.
- 29 M. E. Stewart, N. H. Mack, V. Malyarchuk, J. A. Soares, T. W. Lee, S. K. Gray, R. G. Nuzzo and J. A. Rogers, Quantitative multispectral biosensing and 1D imaging using quasi-3D plasmonic crystals, *Proc. Natl. Acad. Sci. U. S. A.*, 2006, **103**, 17143–17148.
- 30 J. M. Brockman, A. G. Frutos and R. M. Corn, A multistep chemical modification procedure to create DNA arrays on gold surfaces for the study of protein-DNA interactions with surface plasmon resonance imaging, *J. Am. Chem. Soc.*, 1999, **121**, 8044–8051.
- 31 R. Karlsson and A. Fält, Experimental design for kinetic analysis of protein-protein interactions with surface plasmon

- resonance biosensors, *J. Immunol. Methods*, 1997, **200**, 121–133.
- 32 S. M. Marinakos, S. Chen and A. Chilkoti, Plasmonic detection of a model analyte in serum by a gold nanorod sensor, *Anal. Chem.*, 2007, **79**, 5278–5283.
- 33 C. Yu and J. Irudayaraj, Multiplex biosensor using gold nanorods, *Anal. Chem.*, 2007, **79**, 572–579.
- 34 N. A. Cinel, S. Bütün and E. Özbay, Electron beam lithography designed silver nano-disks used as label free nano-biosensors based on localized surface plasmon resonance, *Opt. Express*, 2012, **20**, 2587–2597.
- 35 O. Scholder, K. Jefimovs, I. Shorubalko, C. Hafner, U. Sennhauser and G. L. Bona, Helium Focused Ion Beam Fabricated Plasmonic Antennas with Sub-5 Nm Gaps, *Nanotechnology*, 2013, **24**, 395301.
- 36 T. T. Truong, J. Maria, J. Yao, M. E. Stewart, T. W. Lee, S. K. Gray, R. G. Nuzzo and J. A. Rogers, Nanopost plasmonic crystals, *Nanotechnology*, 2009, **20**, 434011.
- 37 W. Haske, V. W. Chen, J. M. Hales, W. Dong, S. Barlow, S. R. Marder and J. W. Perry, 65 nm feature sizes using visible wavelength 3-D multiphoton lithography, *Opt. Express*, 2007, **15**, 3426–3436.
- 38 H. Fredriksson, Y. Alaverdyan, A. Dmitriev, C. Langhammer, D. S. Sutherland, M. Zäch and B. Kasemo, Hole-mask colloidal lithography, *Adv. Mater.*, 2007, **19**, 4297–4302.
- 39 K. Kim, D. J. Kim, S. Moon, D. Kim and K. M. Byun, Localized surface plasmon resonance detection of layered biointeractions on metallic subwavelength nanogratings, *Nanotechnology*, 2009, **20**, 315501.
- 40 C. Escobedo, On-chip nanohole array based sensing: a review, *Lab Chip*, 2013, **13**, 2445–2463.
- 41 G. Das, E. Battista, G. Manzo, F. Causa, P. A. Netti and E. Di Fabrizio, Large-scale plasmonic nanocones array for spectroscopy detection, *ACS Appl. Mater. Interfaces*, 2015, **7**, 23597–23604.
- 42 S. Tabassum, R. Kumar and L. Dong, Plasmonic crystal-based gas sensor toward an optical nose design, *IEEE Sens. J.*, 2017, **17**, 6210–6223.
- 43 J. T. Gohring, P. S. Dale and X. Fan, Detection of HER2 breast cancer biomarker using the opto-fluidic ring resonator biosensor, *Sens. Actuators, B*, 2010, **146**, 226–230.
- 44 A. Retolaza, J. M. Perdiguero, S. Merino, M. M. Vidal, P. G. Boj, J. A. Quintana, J. M. Villalvilla and M. A. D. Garcia, Organic distributed feedback laser for label-free biosensing of ErbB2 protein biomarker, *Sens. Actuators, B*, 2016, **223**, 261–265.
- 45 Y. Zhang, Y. Zhao, T. Zhou and Q. Wu, Applications and developments of on-chip biochemical sensors based on optofluidic photonic crystal cavities, *Lab Chip*, 2018, **18**, 57–74.
- 46 A. F. Chrimmes, K. Khoshmanesh and P. R. Stoddart, Microfluidics and Raman microscopy: current applications and future challenges, *Chem. Soc. Rev.*, 2013, **42**, 5880–5906.
- 47 Y. Zhang, S. Han, S. Zhang, P. Liu and Y. Shi, High-Q and high-sensitivity photonic crystal cavity sensor, *IEEE Photonics J.*, 2015, **7**, 6802906.
- 48 H. Im, J. N. Sutherland, J. A. Maynard and S. H. Oh, Nanohole-based surface plasmon resonance instruments with improved spectral resolution quantify a broad range of antibody-ligand binding kinetics, *Anal. Chem.*, 2012, **84**, 1941–1947.
- 49 B. Johne, M. Gadnell and K. Hansen, Epitope mapping and binding kinetics of monoclonal antibodies studied by real time biospecific interaction analysis using surface plasmon resonance, *J. Immunol. Methods*, 1993, **160**, 191–198.
- 50 S.-F. Joe, L.-Z. Hsieh, L.-B. Chang and C.-M. Hsu, Wu, C. -M. Kinetic analysis of antibody-antigen interactions using phase-detection-based surface plasmon resonance sensor system, *Jpn. J. Appl. Phys.*, 2007, **46**, 3114.
- 51 Md. A. Ali, S. Tabassum, Q. Wang, Y. Wang, R. Kumar and L. Dong, Plasmonic-electrochemical dual modality microfluidic sensor for cancer biomarker detection, in *Proc. IEEE 30th Int. Conf. Micro Electro Mech. Syst. (MEMS)*, Las Vegas, NV, USA, 2017, pp. 390–393.
- 52 Q. Wang, W. Han, P. Liu and L. Dong, Electrically tunable quasi-3-d mushroom plasmonic crystal, *J. Lightwave Technol.*, 2016, **34**, 2175–2181.
- 53 D. J. Beebe, J. S. Moore, Q. Yu, R. H. Liu, M. L. Kraft, B. H. Jo and C. Devadoss, Microfluidic tectonics: A comprehensive construction platform for microfluidic system, *Proc. Natl. Acad. Sci. U. S. A.*, 2000, **97**, 13488–13493.
- 54 L. Dong, A. K. Agarwal, D. J. Beebe and H. Jiang, Adaptive liquid microlenses activated by stimuli-responsive hydrogels, *Nature*, 2006, **442**, 551–554.
- 55 Md. A. Ali, K. Mondal, Y. Wang, H. Jiang, N. K. Mahal, M. J. Castellano, A. Sharma and L. Dong, In situ integration of graphene foam-titanium nitride based bio-scaffolds and microfluidic structures for soil nutrient sensors, *Lab Chip*, 2017, **17**, 274–285.
- 56 Md. A. Ali, K. Mondal, Y. Jiao, S. Oren, Z. Xu, A. Sharma and L. Dong, Microfluidic immuno-biochip for detection of breast cancer biomarkers using hierarchical composite of porous graphene and titanium dioxide nanofibers, *ACS Appl. Mater. Interfaces*, 2016, **8**, 20570–20582.
- 57 N. Godino, X. Borriese, F. X. Munoz, F. J. Del Campo and R. G. Compton, Mass transport to nanoelectrode arrays and limitations of the diffusion domain approach: theory and experiment, *J. Phys. Chem. C*, 2009, **113**, 11119–11125.
- 58 R. Sharma, Md. A. Ali, N. R. Selvi, V. N. Singh, R. K. Sinha and V. V. Agrawal, Electrochemically assembled gold nanostructures platform: electrochemistry, kinetic analysis, and biomedical application, *J. Phys. Chem. C*, 2014, **118**, 6261–6271.
- 59 N. Tajima, M. Takai and K. Ishihara, Significance of antibody orientation unraveled: well-oriented antibodies recorded high binding affinity, *Anal. Chem.*, 2011, **83**, 1969–1976.
- 60 C. J. Wienken, P. Baaske, U. Rothbauer, D. Braun and S. Duhr, Protein-binding assays in biological liquids using microscale thermophoresis, *Nat. Commun.*, 2010, **1**, 1–7.
- 61 Y. Zhu, P. Chandra and Y.-B. Shim, Ultrasensitive and selective electrochemical diagnosis of breast cancer based

- on a hydrazine–Au nanoparticle–aptamer bioconjugate, *Anal. Chem.*, 2013, **85**, 1058–1064.
- 62 J. T. Gohring, P. S. Dale and X. Fan, Detection of HER2 breast cancer biomarker using the opto-fluidic ring resonator biosensor, *Sens. Actuators, B*, 2010, **146**, 226–230.
- 63 Md. A. Ali, K. Mondal, C. Singh, B. D. Dhar Malhotra and A. Sharma, anti-epidermal growth factor receptor conjugated mesoporous zinc oxide nanofibers for breast cancer diagnostics, *Nanoscale*, 2015, **7**, 7234–7245.
- 64 R. Elshafey, A. C. Tavares, M. Siaj and M. Zourob, Electrochemical impedance immunosensor based on gold nanoparticles– protein G for the detection of cancer marker epidermal growth factor receptor in human plasma and brain tissue, *Biosens. Bioelectron.*, 2013, **50**, 143–149.